

## Excitation mechanisms in moderate-energy $\text{Li}^+$ -Ar collisions

S. Kita<sup>1</sup> and N. Shimakura<sup>2</sup>

<sup>1</sup>*Department of Physics, Nagoya Institute of Technology, Gokiso, Showa-ku, Nagoya 466, Japan*

<sup>2</sup>*Department of Chemistry, Faculty of Science, Niigata University, Ikarashi, Niigata 950-21, Japan*

(Received 11 July 1996)

By means of differential energy-transfer measurements, excitation processes in  $\text{Li}^+$ -Ar collisions have been studied over a wide range of laboratory angles of  $2^\circ \leq \theta \leq 92^\circ$  and at laboratory collision energies of  $70 \leq E_{\text{lab}} \leq 2000$  eV. The  $\text{Li}^+$  and Li atoms scattered inelastically were observed at reduced angles of  $E_{\text{lab}} \theta > 5$  keV deg, and collision energies of  $E_{\text{lab}} \geq 200$  eV. At  $200 \leq E_{\text{lab}} \leq 350$  eV, the inelastic signals are exclusively due to one-electron transitions, while for  $E_{\text{lab}} \geq 500$  eV two-electron excitation as well as one-electron excitation was observed. The electronic transitions in the moderate-energy  $\text{Li}^+$ -Ar collisions take place at distances of  $R < R_c = 0.81$  Å. The excitation mechanism for one-electron charge transfer having the largest cross section is investigated in detail by referring to *ab initio* potentials. The angular dependence of the differential cross sections of two-electron transitions at higher energies shows three different types of excitations: the first transition takes place around  $R_c = 0.75$  Å, the second around  $R_c = 0.47$  Å, and the third around  $R_c = 0.2$  Å. The first and second transitions are due to noncrossing interactions, while the third is attributed to avoided crossing. [S1050-2947(97)03304-0]

PACS number(s): 34.50.Fa, 34.20.Cf

### I. INTRODUCTION

In many experimental and theoretical studies on excitation processes in collisions of closed-shell particles [1–9], the transitions have been shown to depend strongly on the colliding systems. Excitations in low-energy collisions are predominantly due to transitions between states with the same symmetry through nonadiabatic radial coupling, which is classified into avoided-crossing interaction and noncrossing interaction. For symmetric and quasymmetric closed-shell systems, the transitions have a high probability, and are due to potential crossings [3–5]. However, the transitions for most asymmetric closed-shell systems have a very small probability, and are considered to proceed through noncrossing interactions [2,6]. This is also true for quasi-one-electron systems, i.e., alkali-atom–closed-shell-atom systems [7].

Transitions due to potential crossings in low-energy atomic collisions can be well interpreted by the Landau-Zener formula [10]. Excitation through noncrossing interactions has been mostly studied for quasiresonant systems with a small energy defect  $\Delta E$  in the initial and final states [11]. Excitation mechanisms for noncrossing interactions with large  $\Delta E$  in collisions of closed-shell particles have not been studied in detail and are not understood at all, because the transition probability in such systems is so small that the transition mechanisms have been considered to be physically rather less important. In order to understand the excitation mechanisms in the atomic collisions fully, transitions due to noncrossing interactions with large  $\Delta E$  must be investigated in more detail. Such a study of excitation mechanisms in atomic collisions is also of considerable interest in connection with molecular collision dynamics, plasma physics, astrophysics, and surface science.

Differential scattering of  $\text{Li}^+$  ions from Ar atoms has been studied by Barat *et al.* [8] experimentally and theoretically at the energies  $E_{\text{lab}} \geq 500$  eV and the small angles  $\theta < 30^\circ$ . In their experiments, they observed excitations which take

place at a localized internuclear distance, where the excited-state potential curves come to close to the ground-state potential. However, they found that transitions in the  $\text{Li}^+$ -Ar collisions are not due to the avoided-crossing interaction. Considering the avoided crossing between a ground state 1 and an excited state 2, the difference potential  $\Delta E(R) = E_2 - E_1$ , where  $E_i$  denotes the electronic energy of state  $i$ , has a minimum with the separation  $\Delta E = 2V_{12}$  at the crossing distance, where  $V_{12}$  is the interaction energy. In the avoided-crossing case, furthermore, electronic configurations in the wave function interchange with each other around the crossing point. The transition between the two states in collisions with finite velocity takes place exclusively at the crossing distance. The potential crossing is also explained with the diabatic correlation diagram of molecular orbitals (MO's). For  $\text{Li}^+$ -Ar, adiabatic difference potentials  $\Delta E(R)$  have a minimum at  $R \approx 1.5$  a.u., which is close to the critical distance  $R_c$  where electronic transition occurs. According to the MO correlation diagram, however, the ground and lower-lying excited states do not change their electronic configurations around the distance  $R_c$ . Excitations in the moderate-energy  $\text{Li}^+$ -Ar collisions can, therefore, be ascribed to noncrossing interactions. The asymmetric  $\text{Li}^+$ -Ar system is certainly suitable to obtain information on the transitions through noncrossing interactions with large energy defect  $\Delta E$ .

In the  $\text{Na}^+$ -Ar collisions studied previously by us, two different types of excitations have been observed [6]. One is the one-electron transitions taking place at distances of  $R < R_{c1} = 1.07$  Å, and the other is the one- and two-electron transitions occurring at distances of  $R < R_{c2} = 0.45$  Å. These critical distances are close to those of  $|r_i \pm r_j|$  evaluated from the ionic and atomic radii  $r_i$  and  $r_j$ . If this is also true for the  $\text{Li}^+$ -Ar system, the critical distances must be 0.86 and 0.48 Å. As discussed above, transitions at these rather large distances are due to noncrossing interactions. The potentials of the  $\text{Li}^+$ -Ar system, however, also have the avoided crossing

at very small distance [8]. Referring to the diabatic correlation diagram, the crossings in  $\text{Li}^+\text{-Ar}$  are ascribed to a promotion of the  $3d\sigma$  MO, which correlates to the Li  $1s$  atomic orbital (AO). The crossing distance due to  $3d\sigma$  MO promotion is estimated to be around 0.5 a.u. (0.26 Å). In the He-Ar system which is isoelectronic with  $\text{Li}^+\text{-Ar}$ , potential crossings due to the promotion of  $3d\sigma$  MO correlating to a He  $1s$  AO appear at the large distance  $R \approx 1.5$  a.u. (0.79 Å) [9]. Thus the excitational feature is very different between these two isoelectronic systems. Excitations due to  $3d\sigma$  MO promotion have been studied experimentally and theoretically for He-Ar, but have only been predicted for the  $\text{Li}^+\text{-Ar}$  system by the MO correlation diagram.

In this study, differential scattering measurements in the asymmetric  $\text{Li}^+\text{-Ar}$  system have been carried out over a wide range of laboratory angles of  $2^\circ \leq \theta \leq 92^\circ$ ; and at laboratory energies of  $70 \leq E_{\text{lab}} \leq 2000$  eV. Analyzing the velocity of the scattered particles by a time-of-flight technique, excitations over a wide range of internuclear distances have been investigated. In order to obtain information about the excitation mechanisms, *ab initio* potentials of the system have also been computed with a multiconfiguration self-consistent field (MCSCF) method. Our preliminary results for differential scattering in  $\text{Li}^+\text{-Ar}$  collisions at lower energies of  $E_{\text{lab}} \leq 350$  eV have been previously reported [6]. At lower energies, only one-electron transitions are observed, but at energies of  $E_{\text{lab}} \geq 500$  eV two-electron transitions as well as one-electron transitions are observed. The transition probability in the  $\text{Li}^+\text{-Ar}$  system is low compared with that in the isoelectronic He-Ar collisions, because of the different excitation mechanisms. In this paper, we intend to describe completely our experimental results for the  $\text{Li}^+\text{-Ar}$  collisions, their analyses, and MCSCF calculations.

## II. EXPERIMENTS

### A. Apparatus

Differential scattering experiments have been performed with a crossed-beam apparatus. A schematic drawing of the apparatus is shown in Fig. 1. A detailed description of the apparatus has been given previously [12]. The apparatus consists of five chambers: a main chamber, an ion source, a nozzle source followed by a collimation chamber, and a detector chamber. An additional capillary beam source is located in the main chamber. The primary ion beam and secondary (nozzle or capillary) beam cross each other perpendicularly in the main chamber at the scattering center  $O$ , and scattered particles are detected by a rotatable secondary-electron multiplier (Hamamatsu R595).

As is well known, a supersonic molecular beam (nozzle beam) has a narrow velocity spread [13], which is a desirable characteristic to use as a target in the low-energy experiments. At higher collision energies, the differential cross section (DCS) decreases steeply as a function of scattering angle, and the intensity of the scattered particles is extremely low at large angles. Our nozzle beam source provides insufficient intensity for the doubly differential measurements at higher energies and large angles. In this study, the nozzle beam was used as a secondary beam only to measure the total intensity of the scattered particles at higher energies. In order to increase sensitivity at the expense of resolution, the

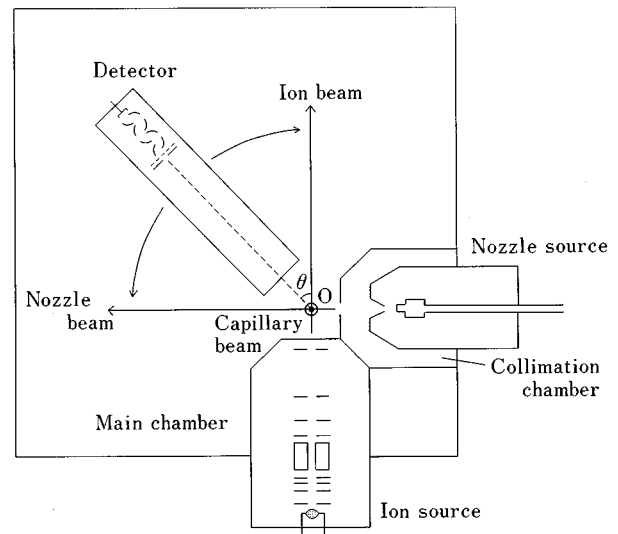


FIG. 1. Schematic drawing of the crossed-beam experiment. The capillary beam is effused from a capillary plate perpendicular to the scattering plane.

capillary beam was effused from a capillary plate (Hamamatsu J5022-01) to cross the primary ion beam perpendicularly at the scattering center  $O$ . The capillary plate is located about 5 mm beneath the scattering center.

The primary  ${}^6\text{Li}^+$  ions are produced by means of thermionic emission from the isotope-enriched  $({}^6\text{Li}_2\text{O})(\text{Al}_2\text{O}_3)(2\text{SiO}_2)$  on a heated platinum wire [14]. The ions are accelerated to the desired energies of  $70 \leq E_{\text{lab}} \leq 2000$  eV, and are collimated by two slits into an angular spread of approximately  $0.07^\circ$  full width at half maximum (FWHM). For time-of-flight (TOF) measurements the ion beam is pulsed with a pair of condenser plates in front of collimating slits [15]. The flight-path length from the scattering center to the detector is approximately 50 cm. The overall angular resolution for the scattered particles is approximately  $0.12^\circ$  FWHM. The time resolution  $\Delta t/t$  (FWHM) in the TOF measurements is approximately  $\frac{1}{800}$  for an ion energy  $E_{\text{lab}} = 2000$  eV at a scattering angle  $\theta = 2^\circ$ . The time resolution at the higher energies is mostly limited by a finite size of scattering volume.

In this apparatus, both ions and neutral atoms scattered into an angle  $\theta$  are detected simultaneously. By sweeping off the scattered ions with a high voltage, only the neutral particles can be detected through the multiplier. Since a negative high voltage ( $V_{\text{EM}} = -2.7$  kV) is usually applied to the first dynode of the multiplier, the positive ions are accelerated to higher energy, and the detection efficiency  $\varepsilon$  for the ions can be estimated to be unity. However, the efficiency  $\varepsilon$  for the neutral atoms, which hit the first dynode with lower velocity, is smaller than unity if the impinging energy  $E_{\text{im}}$  is lower than a critical energy. In order to evaluate the correct intensity of the neutral atoms, one has to determine the detection efficiency  $\varepsilon$  for the atoms. The efficiency  $\varepsilon(\text{Ar})$  for Ar atoms has been determined previously by detecting both  $\text{Na}^+$  ions and Ar atoms scattered elastically in  $\text{Na}^+\text{-Ar}$  collisions [6]. In this experiment, both the neutral Li atoms and  $\text{Ar}^+$  ions produced by charge-exchange reactions were simultaneously detected, so we could evaluate the efficiency

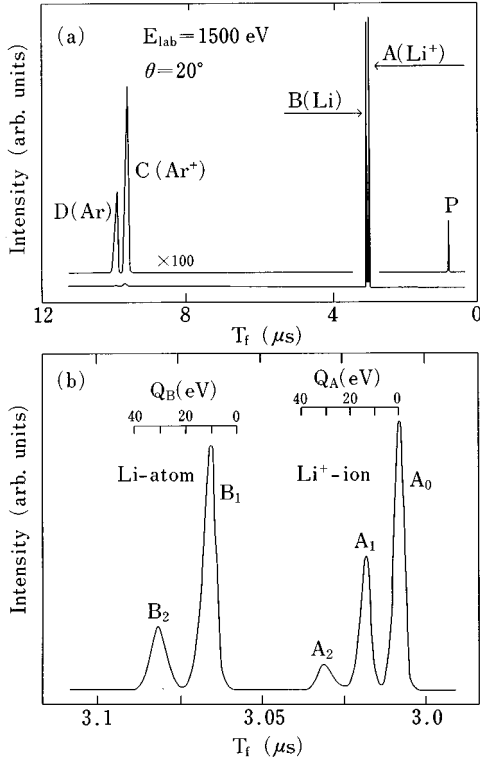


FIG. 2. Typical TOF spectra in the  $\text{Li}^+$ -Ar collisions measured at  $E_{\text{lab}}=1500$  eV and  $\theta=20^\circ$ . (a) Spectrum of all the signals. Peak A is due to the  $\text{Li}^+$  ions, and peak B is ascribed to the Li atoms produced by charge transfers. Peaks C and D are due to the recoiled  $\text{Ar}^+$  ions and Ar atoms, respectively. Weak signal P is ascribed to the photon emitted from the excited Ar and  $\text{Ar}^+$ . Peaks C, D, and P are magnified by a factor of 100. (b) Spectrum of the  $\text{Li}^+$  ions (peaks  $A_0$ ,  $A_1$ , and  $A_2$ ) and the product Li atoms (peaks  $B_1$  and  $B_2$ ). The scales  $Q_A$  and  $Q_B$  denote energy transfers for  $\text{Li}^+$  ions and Li atoms, respectively. Peak  $A_0$  is due to elastic scattering. Peaks  $A_1$  and  $B_1$  are due to one-electron transitions. Peaks  $A_2$  and  $B_2$  are due to two-electron transitions.

$\varepsilon(\text{Li})$  for the Li atoms within the uncertainty of 20% at the energies  $140 < E_{\text{im}} < 1000$  eV. According to the results, the efficiency  $\varepsilon(\text{Li})$  is unity at  $E_{\text{im}} > 700$  eV, and is somewhat higher than  $\varepsilon(\text{Ar})$ .

When a negative high voltage is applied to the first dynode of the multiplier, the negative ions produced in the collisions cannot be detected. The additional TOF measurements, in which the first dynode of the multiplier was grounded, have also been performed to detect the negative ions. In the measurements, the detection efficiency  $\varepsilon$  of the positive ions is estimated to be nearly equal to that of the neutral atoms. On the other hand, the  $\varepsilon$  of the negative ions will be approximately unity, which is almost independent of the impinging energy  $E_{\text{im}}$  under our experimental conditions, because of the electron detachment from the negative ions on the first dynode.

### B. Time-of-flight spectra

Figure 2 shows the typical TOF spectra of the signals detected at the collision energy  $E_{\text{lab}}=1500$  eV and the scattering angle  $\theta=20^\circ$  in the  $\text{Li}^+$ -Ar collisions. The abscissa is the flight time  $T_f$  in units of  $\mu\text{s}$  and the ordinate is the rela-

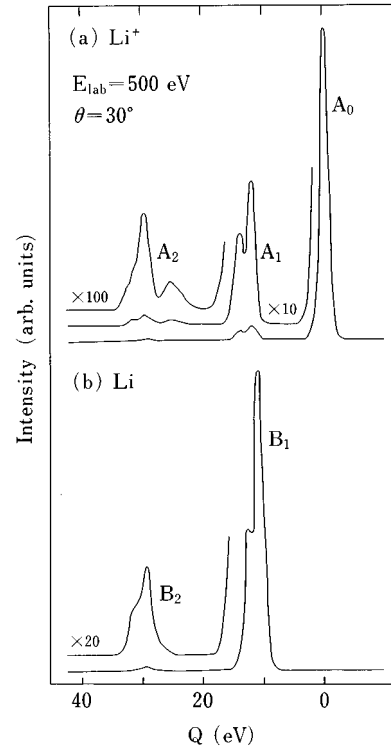
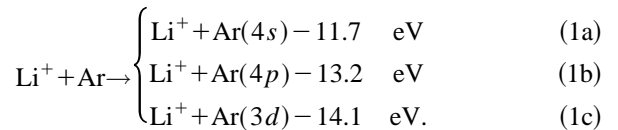


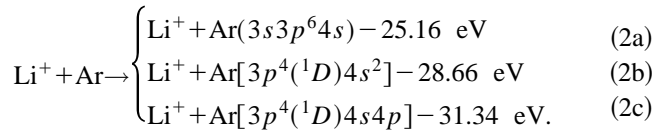
FIG. 3. Energy-transfer spectra in the  $\text{Li}^+$ -Ar collisions measured at  $E_{\text{lab}}=500$  eV and  $\theta=30^\circ$ . (a) Spectrum of the scattered  $\text{Li}^+$  ions. Peak  $A_0$  corresponds to elastic scattering. Peaks  $A_1$  and  $A_2$  are ascribed to one-electron excitation of Ar atoms and excitation of Ar atoms into autoionizing states, respectively. (b) Spectrum of the Li atoms produced by charge-exchange reactions. Peaks  $B_1$  and  $B_2$  are due to one- and two-electron transitions, respectively.

tive intensity. Figure 2(a) displays the spectrum measured with a poor time resolution, and stands for all the observed signals:  $\text{Li}^+$  ions (peak A), Li atoms (B),  $\text{Ar}^+$  ions (C), Ar atoms (D), and photon (P). In Fig. 2(b), only the peaks of the  $\text{Li}^+$  ions ( $A_0$ ,  $A_1$ , and  $A_2$ ) and the Li atoms ( $B_1$  and  $B_2$ ) are shown.

Figure 3 exhibits the energy-transfer spectra measured at  $E_{\text{lab}}=500$  eV and  $\theta=30^\circ$ , where the abscissa is the energy transfer  $Q$  from the kinetic to the excitation energy of the colliding particles in units of eV. In each spectrum, the most intensive peak is normalized to unity. These spectra are deduced from a TOF spectrum by taking into account the Jacobian factor  $dQ/dt$ , where  $t$  means flight time. Peak  $A_0$  of the  $\text{Li}^+$  ions in Fig. 3(a) is due to elastic scattering. Signal  $A_1$  is composed of double peaks and is ascribed to direct excitation of Ar atoms by the reactions

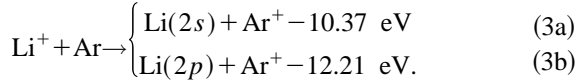


The dominant peak is attributed to reaction (1a), and the lower peak is due to reactions (1b) and (1c). Signal  $A_2$  is also composed of double peaks, which are located around  $Q=25$  and 29 eV. Furthermore, the dominant peak has a shoulder around  $Q=31$  eV. The signal  $A_2$  is attributed to excitations of Ar atoms into the autoionizing states [16]

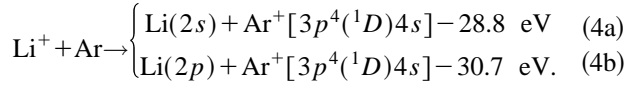


Here reaction (2a) is one-electron process, while reactions (2b) and (2c) are two-electron transitions. The signal due to reaction (2a) could be appreciably observed only at lower energies of  $E_{\text{lab}} < 1000 \text{ eV}$ .

Signal  $B_1$  with double peaks of the Li atoms in Fig. 3(b) is attributed to the charge-exchange reactions of one-electron processes



Signal  $B_2$  with double peaks located around  $Q = 29$  and  $31 \text{ eV}$  will be attributed to the charge-exchange reactions with target excitation



At the energy  $E_{\text{lab}} = 500 \text{ eV}$ , one- and two-electron transitions are observed, but at  $200 \leq E_{\text{lab}} \leq 350 \text{ eV}$  only the one-electron excitations could be found in the spectra. At  $E_{\text{lab}} < 200 \text{ eV}$ , furthermore, inelastic signals could not be appreciably detected.

In the spectrum measured at  $E_{\text{lab}} = 1500 \text{ eV}$  and  $\theta = 20^\circ$  shown in Fig. 2(b), ion peak  $A_1$  located around  $Q = 13.5 \text{ eV}$  is attributed to direct excitation of Ar atoms by reactions (1b) and (1c). Peak  $A_2$  around  $Q = 31 \text{ eV}$  is ascribed to reaction (2c). Atom peak  $B_1$  located around  $Q = 11.5 \text{ eV}$  is due to reactions (3a) and (3b). Peak  $B_2$  at  $Q \approx 31 \text{ eV}$  is mostly attributed to reaction (4b). Under this experimental condi-

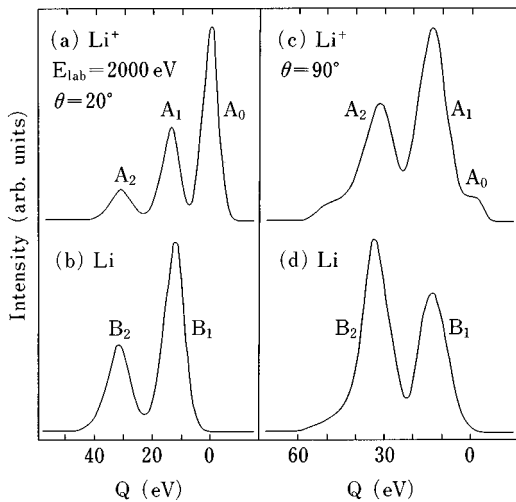


FIG. 4. Energy-transfer spectra measured at  $\theta = 20^\circ$  and  $90^\circ$  for  $E_{\text{lab}} = 2000 \text{ eV}$ . (a) and (c) give spectra of the  $\text{Li}^+$  ions and (b) and (d) are for the produced Li atoms. Peak  $A_0$  corresponds to elastic scattering. Peaks  $A_1$  and  $B_1$  are due to one-electron transitions. Peaks  $A_2$  and  $B_2$  are ascribed to two-electron transitions.

tion, thus, excitation processes with energy transfers somewhat larger than those in Fig. 3 at  $E_{\text{lab}} = 500 \text{ eV}$  and  $\theta = 30^\circ$  are dominant.

Figure 4 shows the energy-transfer spectra of  $\text{Li}^+$  and Li scattered into angles  $\theta = 20^\circ$  and  $90^\circ$  at  $E_{\text{lab}} = 2000 \text{ eV}$ . The spectra of Figs. 4(a) and 4(b) at  $\theta = 20^\circ$  are almost the same as those of Fig. 2(b) at  $\theta = 20^\circ$  and  $E_{\text{lab}} = 1500 \text{ eV}$ . The spectra measured at the large angle  $\theta = 90^\circ$ , however, are remarkably different from the spectra for the small angle  $\theta = 20^\circ$ . In the spectra of Figs. 4(c) and 4(d), elastic peak  $A_0$  is very weak, and two-electron excitation peaks  $A_2$  and  $B_2$  have higher intensity. Furthermore, peak  $A_2$  has a shoulder around  $Q \sim 45 \text{ eV}$ , which could be observed only at large angles of  $\theta > 55^\circ$ . This shoulder will be related to the production of doubly ionized  $\text{Ar}^{2+}$  ions ( $Q = 43.4 \text{ eV}$ ). As can be seen in the spectra, excitation of  $\text{Li}^+$  ions, e.g., into the state of  $\text{Li}^+(1s2s)$  with  $Q = 61 \text{ eV}$ , could not be observed at the energies studied here.

Figure 5 exhibits the probability  $P(\theta)$  of elastic and inelastic scatterings evaluated from the energy-transfer spectra at  $E_{\text{lab}} = 1500 \text{ eV}$ , where  $P(\theta)_i = I(\theta)_i / \sum I(\theta)_i$ , and  $I(\theta)_i$  means the intensity of each peak. There are several exit channels in these high-energy collisions; nevertheless, the probabilities  $P_{A_0}$  of elastic scattering and  $P_{B_1}$  of one-electron charge transfer have clearly resolved oscillating structures, which are in an out-of-phase relation. On the other hand, the  $P(\theta)$ 's for peaks  $A_1$ ,  $B_2$ , and  $A_2$  show only the broader structure.

TOF measurements to detect the negative  $\text{Li}^-$  ions produced in the collisions have also been carried out in this study. However, the additional signal due to the  $\text{Li}^-$  ions could not appreciably be found around the flight time which is expected from the exit channel of  $\text{Li}(2s^2)^- + \text{Ar}^{2+}$  ( $Q = 37.4 \text{ eV}$ ).

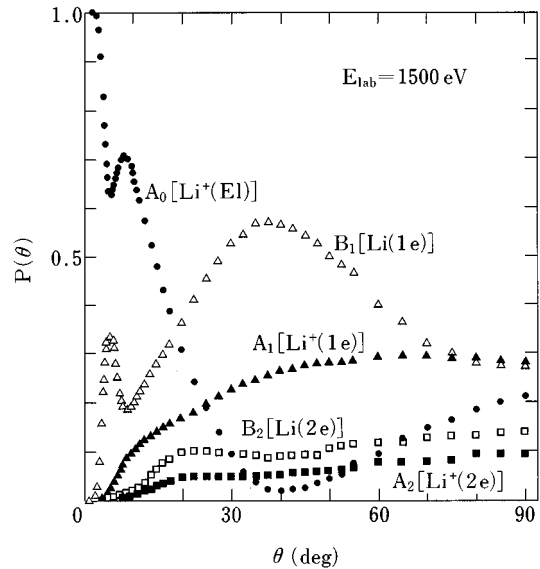


FIG. 5. Angular dependence of the probability  $P(\theta)$  of elastic and inelastic scatterings for  $E_{\text{lab}} = 1500 \text{ eV}$ .  $\bullet$ :  $P_{A_0}$  for the  $\text{Li}^+$  ions scattered elastically.  $\triangle$  and  $\blacktriangle$ :  $P_{B_1}$  for Li atoms and  $P_{A_1}$  for  $\text{Li}^+$  ions, respectively, due to one-electron transitions.  $\square$  and  $\blacksquare$ :  $P_{B_2}$  for Li atoms and  $P_{A_2}$  for  $\text{Li}^+$  ions, respectively, due to two-electron transitions.

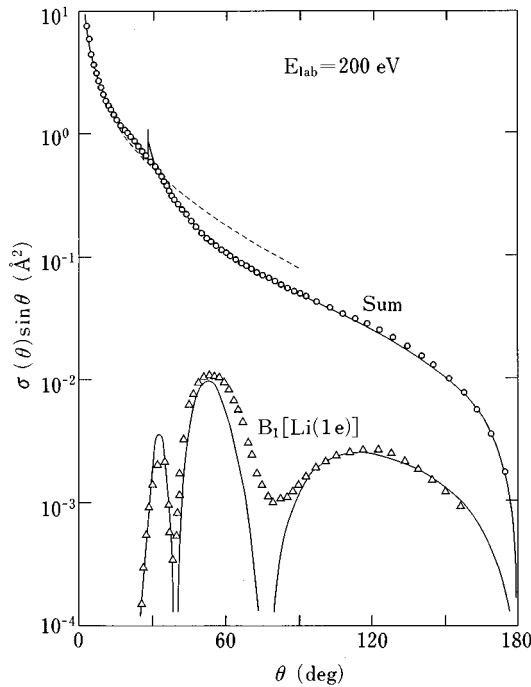


FIG. 6. Angular dependence of the DCS  $\sigma(\theta)\sin\theta$  at  $E_{\text{lab}}=200$  eV.  $\circ$ : sum of the experimental DCS's of the scattered  $\text{Li}^+$  ions and Li atoms.  $\triangle$ : experimental DCS  $\sigma(\theta)_{B1}$  of Li atoms produced by one-electron ( $1e$ ) charge transfer. -----: elastic DCS calculated with the experimental potential of Eq. (5). —: DCS's calculated with the two-state approximation.

### C. Differential cross sections

Angular dependence of the DCS  $\sigma(\theta)\sin\theta$  for the scattered  $\text{Li}^+$  ions and Li atoms at  $E_{\text{lab}}=200$  eV is shown in Fig. 6. Open triangles are the DCS  $\sigma(\theta)_{B1}$  of the Li atoms produced by one-electron charge transfer. At this low energy, the DCS  $\sigma(\theta)_{B1}$  is attributed to reaction (3a), which is the electronic transition into the lowest excited state, and direct excitation of Ar atoms by reaction (1) could not be appreciably observed. Open circles denote sum of the charge-transfer DCS  $\sigma(\theta)_{B1}$  and the elastic DCS  $\sigma(\theta)_{A0}$ ,  $\sigma(\theta)_{\text{sum}} = \sigma(\theta)_{A0} + \sigma(\theta)_{B1}$ . The DCS's  $\sigma(\theta)_{A0}$  and  $\sigma(\theta)_{B1}$  at  $\theta \leq 90^\circ$  were evaluated from the intensity of the  $\text{Li}^+$  ions and Li atoms, respectively. On the other hand, for large angles of  $\theta > 90^\circ$ , the DCS's  $\sigma(\theta)_{B1}$  and  $\sigma(\theta)_{A0}$  were evaluated from the intensity of the  $\text{Ar}^+$  ions and Ar atoms, respectively, recoiled into  $\theta < 45^\circ$ . It must be noted that the Ar atoms and  $\text{Ar}^+$  ions recoiled into a small angle  $\theta$  belong to backward scattering, i.e., a center-of-mass (c.m.) angle  $\Theta \approx \pi - 2\theta$ , because the laboratory angle  $\theta$  is defined here with respect to the beam axis of the primary  $\text{Li}^+$  ions. As can be seen in the figure, the charge-transfer DCS  $\sigma(\theta)_{B1}$  shows a distinctly oscillating structure due to the interference effect. The DCS's for  $E_{\text{lab}}=350$  eV were also evaluated at  $2^\circ \leq \theta \leq 180^\circ$  in the same manner as for  $E_{\text{lab}}=200$  eV.

Figure 7 exhibits DCS's of the  $\text{Li}^+$  ions and Li atoms measured at  $E_{\text{lab}}=500$  eV. The summed DCS for this energy at  $90^\circ < \theta < 180^\circ$  was also deduced from the intensity of Ar atoms and  $\text{Ar}^+$  ions, but the DCS's measured only at angles of  $\theta \leq 90^\circ$  are displayed in the figure. The charge-transfer DCS  $\sigma(\theta)_{B1}$  in Fig. 7 has a distinctly oscillating structure,

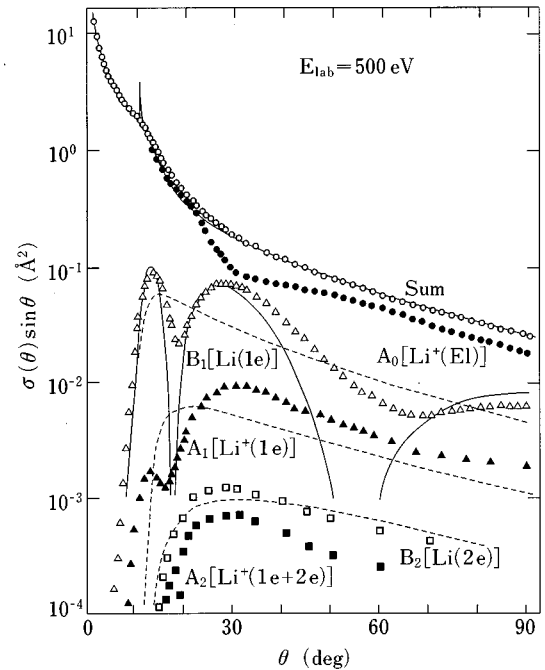


FIG. 7. Angular dependence of the DCS  $\sigma(\theta)\sin\theta$  of the scattered  $\text{Li}^+$  and Li atoms at  $E_{\text{lab}}=500$  eV.  $\circ$  and  $\bullet$ : experimental summed DCS  $\sigma(\theta)_{\text{sum}}$  and elastic DCS  $\sigma(\theta)_{A0}$ , respectively.  $\triangle$  and  $\blacktriangle$ : experimental DCS's  $\sigma(\theta)_{B1}$  and  $\sigma(\theta)_{A1}$ , respectively, of one-electron ( $1e$ ) transitions.  $\square$ : experimental DCS  $\sigma(\theta)_{B2}$  of two-electron ( $2e$ ) transitions.  $\blacksquare$ : experimental DCS  $\sigma(\theta)_{A2}$  of direct excitation of Ar atoms into the autoionizing states. —: DCS's  $\sigma(\theta)_{\text{sum}}$  and  $\sigma(\theta)_{B1}$  calculated with the two-state approximation. -----: DCS's  $\sigma(\theta)_{B1}$ ,  $\sigma(\theta)_{A1}$ , and  $\sigma(\theta)_{B2}$  calculated with the four-state approximation.

the same as for the lower energies  $E_{\text{lab}}=200$  and  $350$  eV. For this energy  $E_{\text{lab}}=500$  eV, the  $\sigma(\theta)_{B1}$  at first maximum is exclusively due to the  $\text{Li}(2s)$  atoms produced by reaction (3a), while at the second maximum the contribution of  $\text{Li}(2p)$  produced by reaction (3b) cannot be ignored, as can be seen in the spectrum of Fig. 3(b). The partial DCS for the product  $\text{Li}(2p)$  evaluated crudely at angles of  $15^\circ < \theta < 45^\circ$  has a broad maximum around  $30^\circ$ , where the partial DCS is approximately 25% of the DCS  $\sigma(\theta)_{B1}$  and is about a factor of 1.5 higher than the DCS  $\sigma(\theta)_{A1}$  of the one-electron excitation of Ar atoms. The DCS  $\sigma(\theta)_{A1}$  also has a distinct structure. The first maximum in  $\sigma(\theta)_{A1}$  is predominantly due to  $\text{Ar}(4s)$  excitation, while, around the second maximum, the contribution of  $\text{Ar}(4p)$  and  $\text{Ar}(3d)$  excitations is remarkable, as can be seen in Fig. 3(a). At large angles of  $\theta \geq 35^\circ$ , the TOF measurements indicate the dominance of  $\text{Ar}(4p)$  and  $\text{Ar}(3d)$ .

The DCS's measured in this study are relative ones. The absolute values of the DCS's for  $E_{\text{lab}}=200$ ,  $350$ , and  $500$  eV were determined by using the integral cross section  $S(\theta_0) = \pi b(\theta_0)^2$  computed with the experimental repulsive potential [17]

$$V(R) = 1750 \exp(-4.24R) \text{ eV}, \quad (5)$$

where  $\theta_0$  means the minimum laboratory angle  $2.0^\circ$  in the DCS measurements,  $b(\theta_0)$  is the impact parameter at the

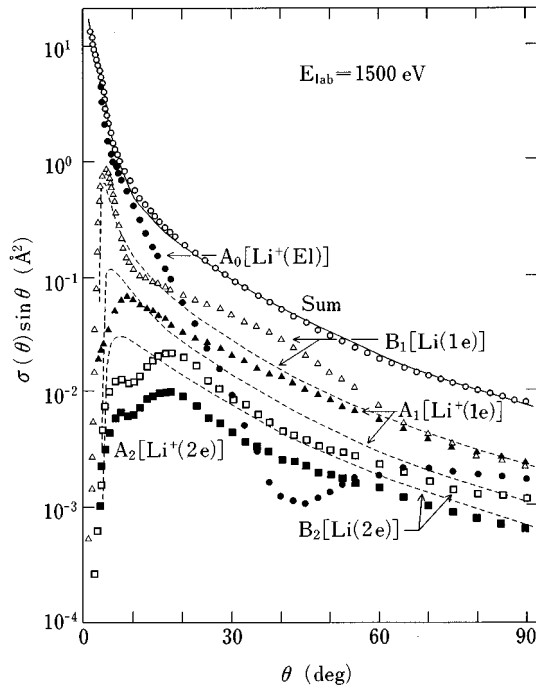


FIG. 8. Angular dependence of the DCS  $\sigma(\theta)\sin\theta$  of  $\text{Li}^+$  ions and Li atoms at  $E_{\text{lab}}=1500$  eV.  $\circ$  and  $\bullet$ : experimental summed DCS  $\sigma(\theta)_{\text{sum}}$  and elastic DCS  $\sigma(\theta)_{A_0}$ , respectively.  $\triangle$  and  $\blacktriangle$ : experimental DCS's  $\sigma(\theta)_{B_1}$  and  $\sigma(\theta)_{A_1}$ , respectively, of one-electron transitions.  $\square$  and  $\blacksquare$ : experimental DCS's  $\sigma(\theta)_{B_2}$  and  $\sigma(\theta)_{A_2}$ , respectively, of two-electron transitions. —: DCS  $\sigma(\theta)_{\text{sum}}$  calculated by assuming elastic scattering. - - -: inelastic DCS's  $\sigma(\theta)_{B_1}$ ,  $\sigma(\theta)_{A_1}$ , and  $\sigma(\theta)_{B_2}$  calculated with the four-state approximation.

angle  $\theta_0$ , and  $R$  is the internuclear distance in units of  $\text{\AA}$ . The normalized results of the DCS's are displayed in Figs. 6 and 7. The dotted curve in Fig. 6 is the elastic DCS calculated with the potential of Eq. (5), which agrees well with the normalized experimental DCS at  $\theta < 30^\circ$ .

Figures 8 and 9 show DCS's of the  $\text{Li}^+$  ions and Li atoms measured at  $E_{\text{lab}}=1500$  and  $2000$  eV, respectively. Since the angular dependence of the DCS's for  $E_{\text{lab}}=2000$  eV at small angles is qualitatively the same as for  $E_{\text{lab}}=1500$  eV, the DCS's only at angles of  $\theta \geq 20^\circ$  are shown in Fig. 9. The solid circles in Fig. 9 are the elastic DCS. The open and solid triangles are the sum of the one-electron excitation DCS's,  $\sigma(\theta)_{1e} = \sigma(\theta)_{A_1} + \sigma(\theta)_{B_1}$ , and of the two-electron excitation DCS's,  $\sigma(\theta)_{2e} = \sigma(\theta)_{A_2} + \sigma(\theta)_{B_2}$ , respectively. The upper scale in Fig. 9 indicates the distance  $R_0$  of closest approach in the collisions. The elastic DCS for  $E_{\text{lab}}=1500$  eV has a distinct minimum around  $\theta=45^\circ$ , while for  $E_{\text{lab}}=2000$  eV the minimum in the elastic DCS is not found clearly. The DCS's  $\sigma(\theta)_{1e}$  and  $\sigma(\theta)_{2e}$  in Fig. 9 are almost parallel at  $\theta < 60^\circ$ , but  $\sigma(\theta)_{2e}$  changes its slope around  $\theta=60^\circ$ , which corresponds to the distance  $R_0 \approx 0.2$   $\text{\AA}$ . As a result, both DCS's have almost the same height at  $\theta > 70^\circ$ .

The angular and energy dependences of the one-electron charge transfer DCS  $\sigma(\theta)_{B_1}$  are exhibited in Fig. 10. Figure 10(a) denotes the DCS measured at energies of  $200 \leq E_{\text{lab}} \leq 2000$  eV. The DCS for  $E_{\text{lab}}=350$  eV was reported previously [6], but the final result is somewhat (20%)

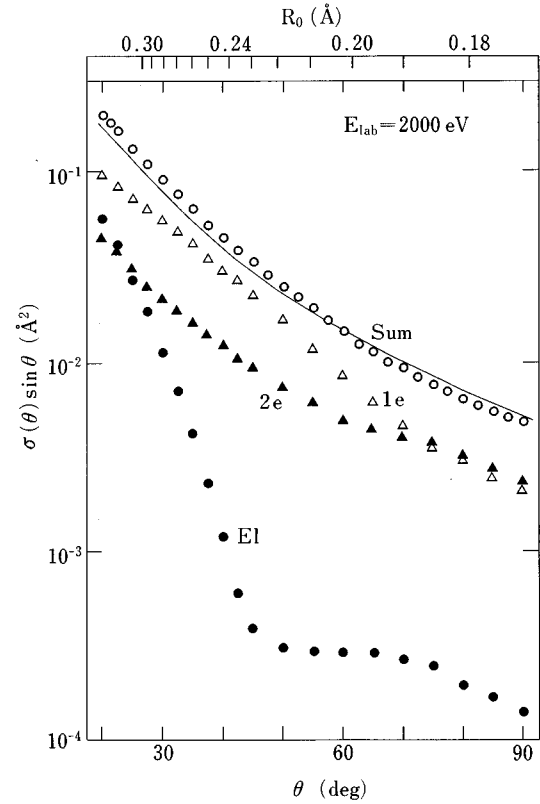


FIG. 9. Angular dependence of the DCS  $\sigma(\theta)\sin\theta$  of  $\text{Li}^+$  ions and Li atoms at  $E_{\text{lab}}=2000$  eV.  $\circ$  and  $\bullet$ : experimental summed DCS's and elastic DCS's, respectively.  $\triangle$  and  $\blacktriangle$ : experimental DCS's of one- and two-electron transitions, respectively. —: summed DCS calculated by assuming elastic scattering. The upper scale  $R_0$  denotes the distance of closest approach in the collisions.

higher than the preliminary results, which is due to the error in the detection efficiency  $\varepsilon(\text{Li})$  of the multiplier determined preliminarily. The transition probability  $P(\theta)_{B_1}$  measured at higher energies has a distinctly oscillatory structure as shown in Fig. 5, but the structure in the DCS  $\sigma(\theta)_{B_1}$  represented by a logarithmic scale is not clear at  $E_{\text{lab}} > 1000$  eV. As can be seen in the figure, the DCS  $\sigma(\theta)_{B_1}$  begins to appear at  $E_{\text{lab}} \theta \approx 5$  keV deg, and has a first maximum around  $E_{\text{lab}} \theta = 6.5$  keV deg, which is almost independent on the energy. For small-angle scattering, the scattering angle  $\theta$  is related to the potential height  $V(R_0)$  at the distance  $R_0$  of closest approach by  $E_{\text{lab}} \theta \approx AV(R_0)$ , where  $A$  is a proportional constant. The experimental results suggest that the one-electron charge transfer takes place at a well-localized distance.

Figure 11 shows the angular and energy dependences of the two-electron ( $2e$ ) charge transfer DCS  $\sigma(\theta)_{B_2}$  measured at the energies  $E_{\text{lab}} \geq 500$  eV. As can be seen in Figs. 7 and 8, the DCS  $\sigma(\theta)_{B_2}$  has, roughly say, the angular and energy dependences similar to those of the DCS  $\sigma(\theta)_{A_2}$  for the direct excitation of Ar atoms into the autoionizing states. However, the DCS  $\sigma(\theta)_{B_2}$  is larger than  $\sigma(\theta)_{A_2}$  approximately by factors of 1.5–3.5, except at the large angles  $\theta > 70^\circ$  for  $E_{\text{lab}}=2000$  eV where both DCS's have almost the same magnitude.

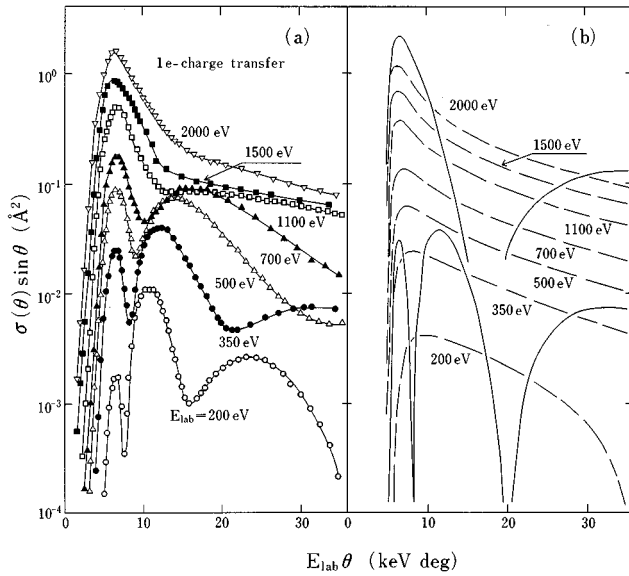


FIG. 10. Angular and energy dependences of the DCS  $\sigma(\theta)_{B1}$  of one-electron charge transfer. (a) Experimental DCS.  $\circ$ : 200 eV.  $\bullet$ : 350 eV.  $\triangle$ : 500 eV.  $\blacktriangle$ : 700 eV.  $\square$ : 1100 eV.  $\blacksquare$ : 1500 eV.  $\nabla$ : 2000 eV. Solid curves are drawn to guide the eye. (b) Calculated DCS. —: calculations with the interference effect for  $E_{lab}=350$  and 2000 eV. - -: calculations without the interference effect for energies of  $200 \leq E_{lab} \leq 2000$  eV.

### III. ANALYSES OF EXPERIMENTAL RESULTS

#### A. Ground-state potential

Excitation in the  $\text{Li}^+-\text{Ar}$  collisions is observed distinctly at energies of  $E_{lab} \geq 200$  eV, but the transition probability is

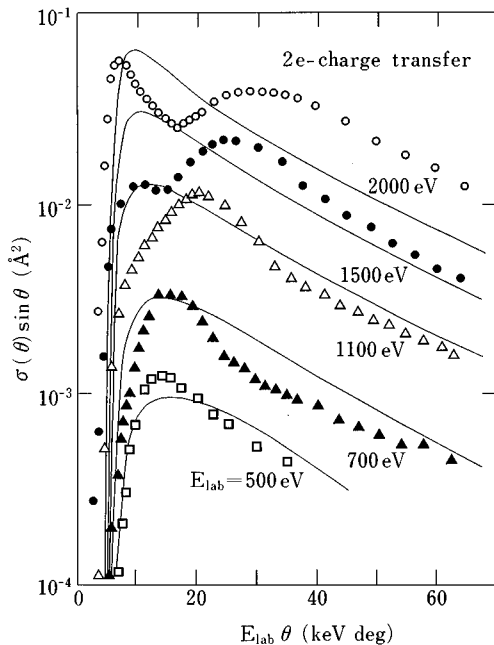


FIG. 11. Angular and energy dependences of the DCS  $\sigma(\theta)_{B2}$  of the two-electron charge transfer.  $\square$ : experimental DCS at  $E_{lab}=500$  eV.  $\blacktriangle$ : for 700 eV.  $\triangle$ : for 1100 eV.  $\bullet$ : for 1500 eV.  $\circ$ : for 2000 eV. —: DCS calculated with the four-state approximation.

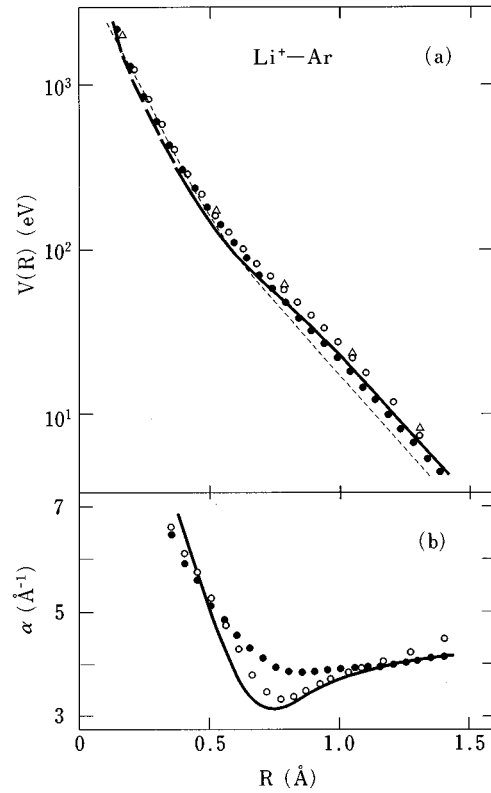


FIG. 12. (a) Ground-state potentials. — and - -: experimental potentials deduced by the inversion and curve-fitting procedures, respectively.  $\circ$  and  $\bullet$ : calculations with the MCSCF method and the statistical electron-gas model, respectively.  $\triangle$ : calculation by Barat *et al.* (Ref. [8]). - - - -: empirical model potential. (b) Potential gradient on the logarithmic scale. —: experimental result.  $\circ$  and  $\bullet$ : MCSCF and statistical calculations, respectively.

still small at lower energies of  $E_{lab} \leq 500$  eV. The ground-state potential, which is needed for a quantitative discussion of excitation mechanisms in the collisions, was directly evaluated from the summed DCS determined experimentally at angles of  $2.0^\circ \leq \theta \leq 180^\circ$  for  $E_{lab}=200, 350,$  and  $500$  eV by employing the inversion method developed by Firsov [18]. Direct inversion needs the DCS over the full angular range in the c.m. system ( $0^\circ \leq \Theta \leq 180^\circ$ ). The DCS at small angles of  $\theta < 2.0^\circ$  was evaluated here by using the experimental potential of Eq. (5). As seen in Figs. 6 and 7, inelastic DCS's depend strongly on the collision energy, nevertheless the inversion results deduced from the three energies agree within 5%. This suggests that the potential deduced here is sufficiently accurate. The solid curve in Fig. 12(a) displays the potential deduced with the inversion method at  $4 < V(R) < 300$  eV ( $0.38 \leq R \leq 1.43$  Å). The inversion results can be approximately fitted to an analytical form

$$V(R) = 1750 \exp(-4.24R) - (9.549R)^9 \exp(-19.8R) \text{ eV} \quad (6)$$

within an error of 3%, where the first term on the right-hand side equals the experimental potential of Eq. (5).

As can be seen in Fig. 12(a), the ground-state potential does not lie on a straight line on the logarithmic scale, but shows an inclination structure, which is similar to the poten-

tial for  $\text{Na}^+\text{-Ar}$  determined previously [6]. The solid curve in Fig. 12(b) represents the potential gradient  $\alpha(R) = -d \ln V(R)/dR$ , deduced from the inversion results, which has a minimum value of  $\alpha \approx 3.15 \text{ \AA}^{-1}$  at  $R \approx 0.75 \text{ \AA}$ .

At higher energies and large angles, as seen in Fig. 8, the probability of the elastic scattering is very small. However, as will be discussed below, the ratio  $\Delta V/V$  of the potential difference  $\Delta V$  between the ground and excited states to the ground-state potential  $V$  is small at smaller distances. Then a crude potential was also evaluated from the summed DCS measured at  $700 \leq E_{\text{lab}} \leq 1500 \text{ eV}$  by the curve fitting of the DCS, with the potential of Eq. (6) at larger distances. The solid curve in Fig. 8 shows the fitting result of the summed DCS. Thus the calculation reproduces sufficiently the experimental summed DCS. The deduced potential is given by

$$V(R) = 1750 \exp(-4.24R) - (9.549R)^9 \exp(-19.8R) + 13\,000 \exp(-18R) \text{ eV.} \quad (7)$$

The broken curve at small distances in Fig. 12(a) exhibits the potential given by Eq. (7). The solid curve in Fig. 9 also gives the summed DCS at  $E_{\text{lab}} = 2000 \text{ eV}$  calculated with Eq. (7) by assuming elastic scattering.

## B. Excited-state potentials

In the moderate-energy  $\text{Li}^+\text{-Ar}$  collisions, one- and two-electron excitations having nearly the same threshold angle are observed at  $E_{\text{lab}} \geq 500 \text{ eV}$ . However, one-electron charge-transfer DCS  $\sigma(\theta)_{B1}$  has the largest height among the inelastic DCS's at  $E_{\text{lab}} \theta \leq 90 \text{ keV deg}$ , and also shows a distinctly oscillating structure due to the interference effect. The oscillatory structure in the DCS provides information about the difference potential  $\Delta V$  between the ground and excited states [19]. In this study, therefore, the excited-state potential for reaction (3a) as well as the ground-state potential was first evaluated by the curve fitting of the DCS  $\sigma(\theta)_{B1}$ , assuming a two-state approximation. The dominant two-electron process in the  $\text{Li}^+\text{-Ar}$  collisions is due to charge transfer with target excitation. Then the excited-state potential for the charge-exchange reaction (4) of the two-electron process was estimated by the curve fitting of the DCS  $\sigma(\theta)_{B2}$ , assuming a four-state approximation. Here we will discuss the one- and two-electron transitions separately.

### 1. One-electron charge transfer

Electronic transitions in the  $\text{Li}^+\text{-Ar}$  collisions are due to noncrossing interactions rather than the crossing interaction [8]. However, the measured angular and energy dependences of the one-electron charge transfer in Fig. 10(a) indicate that the transition takes place at a well-localized distance. As an approximate treatment, then, the elastic and excitation DCS's were calculated by using the formula for the Landau-Zener transition probability at the critical (crossing) distance modified by Zhu and Nakamura [20],

$$p = \exp(-2\pi V_{12}^2 f / \hbar v_r \Delta S), \quad (8a)$$

with

$$f = [2/(1 + \sqrt{1 + (0.70 + 0.40a^2)b^{-4}})]^{1/2}, \quad (8b)$$

TABLE I. The crossing parameters for one-electron charge transfer deduced from the experiments and from the *ab initio* MCSCF potentials. The definitions of MCSCF1 and MCSCF2 are given in the text.

	$R_c$ ( $\text{\AA}$ )	$V(R_c)$ (eV)	$V_{12}$ (eV)	$V_{12}^2/\Delta S$ (eV $\text{\AA}$ )
Expt.	0.810	47.0	2.57	0.240
MCSCF1	0.774	63.2	2.24	0.145
MCSCF2	0.875	43.3	2.88	0.244

where  $V_{12}$  is the interaction energy between the ground and excited states,  $\Delta S$  is the difference in slopes of the two potential curves  $V_1$  and  $V_2$ , and  $v_r$  is the radial velocity. According to close-coupling calculations, the transition probability  $p$  must have a finite value even if the distance  $R_0$  at closest approach is equal to the crossing distance  $R_c$ . The original Landau-Zener formula [10], however, gives  $p = 0$  at  $R_0 = R_c$ , and is not a good approximation at  $R_0 \approx R_c$ . The quantity  $f$  in Eq. (8) is a correction factor for the Landau-Zener formula around the crossing distance, and  $a$  and  $b$  in factor  $f$  are the diabatic parameters,  $(ab)^{-1} = 8V_{12}^2/\hbar v_r \Delta S$ .

In the fitting procedure, diabatic ground- and excited-state potentials were initially estimated by referring to the ground-state potential of Eq. (7). Taking into account the interference effect, the semiclassical DCS  $\sigma(\theta)_{B1}$  was calculated iteratively as a function of the potential parameters and of the interaction energy  $V_{12}$  at the critical distance to obtain a best fit of the DCS  $\sigma(\theta)_{B1}$  measured at energies of  $200 \leq E_{\text{lab}} \leq 500 \text{ eV}$ .

The solid curves in Figs. 6 and 7 represent the fitting results of the summed and charge-transfer DCS's. The calculations reproduce fairly well the overall features of the experiments. The solid curves in Fig. 10(b) also show the charge-transfer DCS calculated semiclassically at  $E_{\text{lab}} = 350$  and  $2000 \text{ eV}$ . The broken curves in Fig. 10(b) also exhibit the angular and energy dependences of the DCS  $\sigma(\theta)_{B1}$  calculated without the interference effect at energies of  $200 \leq E_{\text{lab}} \leq 2000 \text{ eV}$ . Both calculations again reasonably reproduce the experiments. The diabatic ground- and excited-state potentials deduced experimentally are

$$V_1 = 1750 \exp(-4.24R) - (9.581R)^9 \exp(-20R) + 13\,000 \exp(-18R) \text{ eV} \quad (9a)$$

and

$$V_2 = 1912 \exp(-4.60R) - (9.581R)^9 \exp(-20R) - (25.12R)^5 \exp(-25R) + 13\,000 \exp(-18R) + 10.4 \text{ eV.} \quad (9b)$$

The potential parameters at the crossing point, which characterize the electronic transition, are listed in Table I.

At higher collision energies, there exist several exit channels, nevertheless the probabilities  $P_{A0}$  for the elastic scattering and  $P_{B1}$  for the one-electron charge transfer in Fig. 5 for  $E_{\text{lab}} = 1500 \text{ eV}$  oscillate out of phase. This suggests that the two-state approximation can be applied to estimate the

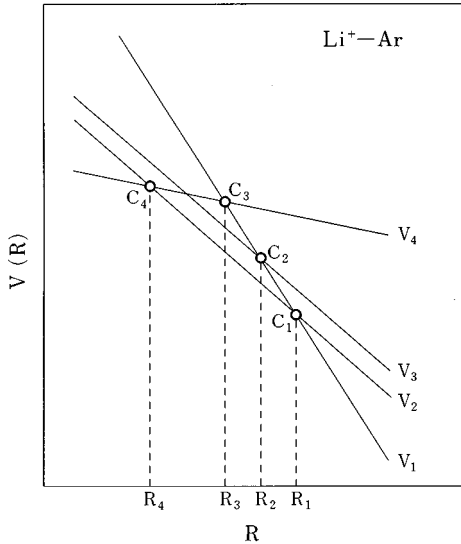


FIG. 13. Schematic drawing of the diabatic potentials for  $\text{Li}^+\text{-Ar}$ .  $V_1$ ,  $V_2$ ,  $V_3$ , and  $V_4$  are the potentials for the ground-state, one-electron charge transfer, one-electron excitation of Ar atoms, and two-electron charge transfer, respectively. For two-electron charge transfer, the transition is assumed to take place through crossing  $C_3$  (or  $C_4$ ), but particles diabatically path through crossing  $C_4$  (or  $C_3$ ).

potential difference  $\Delta V = V_2 - V_1$  at smaller distances. The probability  $P(\theta)_{B1}$  calculated with the potentials of Eq. (9) has a second maximum around  $\theta = 28^\circ$ , which is smaller than the experimental angle  $\theta = 40^\circ$ . This is due to the fact that the difference  $\Delta V$  given by Eq. (9) at the smaller distance  $R \sim 0.3 \text{ \AA}$  is somewhat too large. So, with the ground-state potential of Eq. (9a) being kept the same, we corrected the potential  $V_2$  of Eq. (9b) to better reproduce the second maximum location in  $P(\theta)_{B1}$ . The result is given by

$$V_2 = 1912 \exp(-4.60R) - (9.581R)^9 \exp(-20R) \\ - (24.02R)^5 \exp(-25R) + 13\,000 \exp(-18R) \\ + 10.4 \text{ eV.} \quad (10)$$

In this potential, the preexponential constant in the third term is a little smaller than that for Eq. (9b).

## 2. Charge transfer with target excitation

A schematic drawing of the diabatic potentials employed in the data analyses is represented in Fig. 13. The charge transfer and excitation of Ar atoms of one-electron processes are assumed to take place through the crossings  $C_1$  and  $C_2$ , respectively. Since the excitation mechanisms in the largely asymmetric  $\text{Li}^+\text{-Ar}$  system is not clear, the two-electron transition was analyzed with two different models in this study. In models 1 and 2 the transition was assumed to proceed through the crossings  $C_3$  and  $C_4$ , respectively, but the particles diabatically passed through the crossings  $C_4$  and  $C_3$ , respectively. The excited-state potentials  $V_2$ ,  $V_3$ , and  $V_4$  as well as the ground-state potential  $V_1$  were evaluated by the curve fitting of the excitation DCS's  $\sigma(\theta)_{A1}$ ,  $\sigma(\theta)_{B1}$ , and  $\sigma(\theta)_{B2}$ . Taking into account the overall features of the excitation DCS's the fitting was performed at  $E_{\text{lab}} = 500$  and 700

TABLE II. The crossing parameters deduced from the experiments by assuming four-state approximation.

Parameter	$C_1$	$C_2$	$C_3$ (model 1)	$C_4$ (model 2)
$R_c$ ( $\text{\AA}$ )	0.860	0.803	0.739	0.750
$V(R_c)$ (eV)	42.2	52.4	66.4	59.8
$\Delta S$ (eV/ $\text{\AA}$ )	30.9	32.4	85.1	62.7
$V_{ij}$ (eV) <sup>a</sup>	2.80	2.35	3.70	6.00
$\Sigma V_{ij}$ (eV) <sup>b</sup>	2.80	5.15	8.85	8.80

<sup>a</sup> $V_{ij} = V_{12}$  for  $C_1$ ,  $V_{13}$  for  $C_2$ ,  $V_{14}$  for  $C_3$ , and  $V_{24}$  for  $C_4$ .

<sup>b</sup> $\Sigma V_{ij} = V_{12}$  for  $C_1$ ,  $V_{12} + V_{13}$  for  $C_2$ ,  $V_{12} + V_{13} + V_{14}$  for  $C_3$ , and  $V_{12} + V_{24}$  for  $C_4$ .

eV. In the fitting procedure, the excitation DCS's were calculated without the interference effect by using the transition probability of Eq. (8) at each crossing point.

The dotted curves in Fig. 7 display the fitting results of the excitation DCS's  $\sigma(\theta)_{A1}$ ,  $\sigma(\theta)_{B1}$ , and  $\sigma(\theta)_{B2}$ . The one-electron charge-transfer DCS  $\sigma(\theta)_{B1}$  in the figure is almost the same as that of the two-state approximation calculated without the interference effect. The fitting results of the DCS  $\sigma(\theta)_{B2}$  with two different models mutually agree within 20% at the angular range shown in the figure, so the averaged result is represented in Fig. 7. Although the simple model potentials were used in the analysis, the fitting results for  $E_{\text{lab}} = 500$  and 700 eV fairly reproduce the overall features of the excitation DCS's. The crossing parameters deduced from the experimental excitation DCS's are given in Table II. The interaction energy  $V_{14} = 3.70$  eV at the crossing  $C_3$  obtained with model 1 is different from  $V_{24} = 6.00$  eV at  $C_4$  in model 2, but the sum of  $V_{12} + V_{13} + V_{14} = 8.85$  eV for  $C_3$  is nearly equal to  $V_{12} + V_{24} = 8.80$  eV for  $C_4$ .

The dotted curves in Fig. 8 exhibits the excitation DCS's  $\sigma(\theta)_{A1}$ ,  $\sigma(\theta)_{B1}$ , and  $\sigma(\theta)_{B2}$  for  $E_{\text{lab}} = 1500$  eV calculated with the potential parameters deduced from the experiments at  $E_{\text{lab}} = 500$  and 700 eV. The calculations reproduce only crudely the experiments. The solid curves in Fig. 11 represent the angular and energy dependences of the DCS  $\sigma(\theta)_{B2}$  of the charge transfer with target excitation. The calculations reproduce satisfactorily the gross features of the experiments. As shown in Fig. 11, however, the DCS  $\sigma(\theta)_{B2}$  has a maximum at lower energies but has double maxima at the higher energies  $E_{\text{lab}} = 1500$  and 2000 eV, which cannot be explained at all by the model potentials used here. The discrepancy will be discussed below.

## IV. COMPUTATION OF REPULSIVE POTENTIALS

In order to elucidate the excitation mechanisms in the  $\text{Li}^+\text{-Ar}$  collisions, *ab initio*  $^1\Sigma^+$  potentials of singly and doubly excited states as well as the  $^1\Sigma^+$  ground-state potential have been computed at the internuclear distances of  $0.35 \leq R \leq 20$  a.u. with the multiconfiguration self-consistent field (MCSCF) method. The computations were carried out with the quantum-chemistry code GAMESS revised by Schmidt *et al.* [21]. The active space of the MCSCF computations includes all valence orbitals and electrons. In the calculations, we used the McLean-Chandler extended basis set [22] augmented by double sets of six *d* functions for Li and Ar atoms. The orbital exponents of the polarization functions

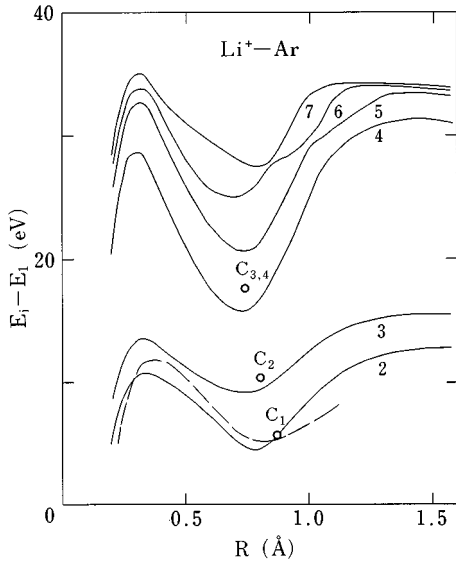


FIG. 14. Adiabatic difference potentials of the excited states. —: MCSCF calculations. - -: experimental potentials of first excited state 2. ○: experimental potentials at the critical distances  $C_1$ ,  $C_2$ , and  $C_3$  (or  $C_4$ ).

are 0.1 and 0.4 for the Li atom, and 0.425 and 1.7 for the Ar atom. Our basis set has, therefore, the quality of triple  $\zeta$  plus double polarizations. The ground-state potential has also been calculated with the statistical electron-gas model [23], which provides reasonably reliable repulsive potentials for closed-shell particles.

The open and solid circles in Fig. 12(a) show the ground-state potentials calculated with the MCSCF method and the statistical model, respectively. The open triangles are the results computed with a single-configuration approximation of self-consistent-field method with molecular orbitals constructed by linear combination of Slater-type atomic orbitals by Barat *et al.* [8]. The dotted curve gives the potential evaluated with an empirical overlap model [24] by using the electron density that was obtained from the analytical wave functions. As can be seen in the figure, all the calculations

agree reasonably well with the experiments. The open and solid circles in Fig. 12(b) display the gradient  $\alpha = -d \ln V(R)/dR$  on a logarithmic scale evaluated from the MCSCF potentials and the statistical calculations, respectively. The *ab initio* potentials give a minimum value of  $\alpha_m \approx 3.35 \text{ \AA}^{-1}$  around  $R_{\text{inc}} = 0.77 \text{ \AA}$ , which is similar to the experiment, while the statistical calculation has only a shallow minimum at  $R_{\text{inc}} = 0.85 \text{ \AA}$ . The inclination point in the experimental and theoretical potentials,  $R_{\text{inc}} = 0.75\text{--}0.85 \text{ \AA}$ , is nearly equal to the critical distances  $R_c = 0.74\text{--}0.86 \text{ \AA}$  for the one- and two-electron transitions deduced from the experiments in Tables I and II. Thus the inclination point  $R_{\text{inc}}$  in the ground-state potential for the asymmetric  $\text{Li}^+\text{-Ar}$  system has a close relation to the critical distances  $R_c$ 's, which is the same as for  $\text{Na}^+\text{-Ar}$  [6].

The solid curves in Fig. 14 represent the adiabatic difference potentials  $\Delta E = E_i - E_1$  for the  $\text{Li}^+\text{-Ar}$  system obtained by the MCSCF calculations, where  $E_i$  and  $E_1$  are the electronic energies of the system for excited state  $i$  and ground state 1, respectively. In this figure we show only the difference potentials of the two lowest excited-states and the four highly excited states, which are closely related to our discussion. Since the computations were mostly performed with an interval of 0.1 a.u., the curves in the figure are the interpolated results. The main configurations in the wave functions of the states shown in Fig. 14 at the specific distances are listed in Table III.

In an avoided crossing between states  $i$  and  $j$ , the adiabatic difference potential  $\Delta E = E_j - E_i$  is related to the diabatic potential  $|\Delta V| = |V_j - V_i|$  by [25]

$$\Delta E = 2 \sqrt{(\Delta V/2)^2 + V_{ij}^2} \quad (11a)$$

and

$$|\Delta V| = 2 \sqrt{(\Delta E/2)^2 - V_{ij}^2}. \quad (11b)$$

The broken curve in Fig. 14 denotes the adiabatic difference potential  $\Delta E = E_2 - E_1$  evaluated from the experimental diabatic potentials  $V_1$  and  $V_2$  of Eqs. (9) and (10), with  $V_{12} = 2.57 \text{ eV}$ . The curve deduced from the experiments is a little higher than the MCSCF curve 2, and is shifted to some-

TABLE III. Main configurations in the MCSCF wave functions of states at specific distances of 0.4, 1.4, and 20 a.u.

State	Distance $R$ (a.u.)		
	0.4	1.4	20
1	$\text{Li}^+ + \text{Ar}(3p^6)$	$\text{Li}^+ + \text{Ar}(3p^6)$	$\text{Li}^+ + \text{Ar}(3p^6)$
2	$\text{Li}(2s) + \text{Ar}^+(3s3p^6)$	$\text{Li}(2s) + \text{Ar}^+(3p^5)$	$\text{Li}(2s) + \text{Ar}^+(3p^5)$
3	$\text{Li}^+ + \text{Ar}(3s3p^64s)$	$\text{Li}^+ + \text{Ar}(3p^54s)$	$\text{Li}^+ + \text{Ar}(3p^54s)$
4	$\text{Li}^-(2s^2) + \text{Ar}^{2+}(3s^03p^6)$ $\text{Li}^-(2s^2) + \text{Ar}^{2+}(3s3p^5)$	$\text{Li}^-(2s^2) + \text{Ar}^{2+}(3p^4)$	$\text{Li}(2s) + \text{Ar}^+(3s3p^6)$
5	$\text{Li}(2s) + \text{Ar}^+(3s3p^54s)$ $\text{Li}(2s) + \text{Ar}^+(3s^03p^64s)$	$\text{Li}(2s) + \text{Ar}^+(3p^44s)$	$\text{Li}^+ + \text{Ar}(3s3p^64s)$
6	$\text{Li}(2s) + \text{Ar}^+(3p^5)$	$\text{Li}^+ + \text{Ar}(3p^44s^2)$	$\text{Li}(2s) + \text{Ar}^+(3p^44s)$
7	$\text{Li}^+ + \text{Ar}(3s3p^64s)$ $\text{Li}^+ + \text{Ar}(3s3p^54s^2)$ $\text{Li}^+ + \text{Ar}(3s^03p^64s^2)$	$\text{Li}(2s) + \text{Ar}^+(3s3p^6)$	$\text{Li}(2s) + \text{Ar}^+(3p^44s)$
8	$\text{Li}^+ + \text{Ar}(3p^54s)$	$\text{Li}^+ + \text{Ar}(3s3p^64s)$	$\text{Li}^+ + \text{Ar}(3p^44s^2)$

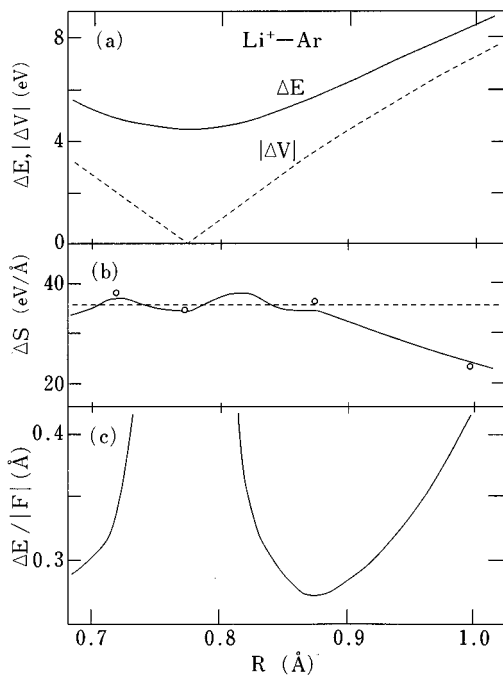


FIG. 15. (a) Adiabatic and diabatic MCSCF potentials of state 2. —: adiabatic potential. ----: diabatic potential. (b) Difference in slopes of diabatic potentials 1 and 2. —: direct evaluation. ○: evaluation in the manner of Zhu and Nakamura (Ref. [20]). ----: averaged value at  $R < 0.88$  Å. (c) Inverse of the gradient  $\beta = |d \ln \Delta E / dR|$  of the difference potential  $\Delta E$  on the logarithmic scale.

what larger distances. The open circles  $C_1$ ,  $C_2$ , and  $C_3$  (or  $C_4$ ) are the adiabatic potential difference  $\Delta E = 2 \sum V_{ij}$  evaluated roughly with the sum of the interaction energies  $\sum V_{ij}$  given in Table II at the crossing points  $C_1$ ,  $C_2$ , and  $C_3$  (or  $C_4$ ), respectively. The open circle  $C_1$  is just on the MCSCF curve 2. The open circle  $C_2$  is also close to the *ab initio* curve 3, while the open circle  $C_3$  (or  $C_4$ ) is located between curves 4 and 5.

## V. DISCUSSION

Assuming an avoided crossing, the relation between the adiabatic and diabatic difference potentials is given by Eq. (11). Then, one can evaluate the crossing parameters from the theoretical adiabatic potential curves. Since the crossing parameters given in Table I are deduced from the predominant charge-transfer DCS having a distinctly oscillating structure, these experimental values are considered to be most reliable to compare them with the calculations. We will first discuss the mechanism for charge-exchange reaction of one-electron process.

### A. One-electron charge transfer

The solid curve in Fig. 15(a) again gives the adiabatic potential  $\Delta E = E_2 - E_1$ , which is the same as curve 2 in Fig. 14, at a limited range of distance. The potential has a minimum value of  $\Delta E_{\min} = 4.48$  eV at  $R_{\min} = 0.774$  Å. The dotted curve in the figure exhibits the diabatic potential  $|\Delta V| = |V_2 - V_1|$  evaluated by Eq. (11b) with

$V_{12} = \Delta E_{\min} / 2 = 2.24$  eV at  $R_{\min} = R_c = 0.774$  Å. The absolute value of the slope of the difference potentials  $\Delta S = |d \Delta V / dR|$  directly obtained from the diabatic potential curve in Fig. 15(a) is displayed in Fig. 15(b) by a solid curve. The calculated  $\Delta S$  is almost constant fluctuating weakly around 35.5 eV/Å (dotted curve in the figure) at  $R < 0.88$  Å. The fluctuation is probably due to less input-data points. As can be seen in the figure, at  $R > 0.88$  Å  $\Delta S$  decreases with increasing distance  $R$ . Open circles in the figure are the values estimated with the formula by Zhu and Nakamura [20]. Both evaluations give almost the same results. The potential parameters cited as MCSCF1 in Table I are the values estimated from the *ab initio* potential with the manner mentioned here. As seen in the table, the critical distance  $R_c$  obtained from the MCSCF potential is somewhat smaller than the experimental value, so the evaluated  $V(R_c)$  is approximately 35% higher than the experiment. The evaluated parameter  $V_{12}^2 / \Delta S$ , which determines the transition probability, furthermore, is approximately 40% smaller than the experiment. These differences in the crossing parameters provide significant errors in the threshold angle and the magnitude of the charge-transfer DCS. This suggests that the distance  $R_c$  is not the minimum location  $R_{\min}$  in the difference potential  $\Delta E$ , but somewhat larger than it. The analysis of the *ab initio* potential with the manner for the avoided crossing, thus, cannot sufficiently reproduce the experimental potential parameters at the critical distance  $R_c$ .

As discussed above, the inclination point  $R_{\text{inc}}$  in the ground-state potential is close to the crossing distances determined experimentally. In a similar way, we assume here that an extremum point in the gradient of the difference potential  $\Delta E$ ,  $\beta = |d \ln \Delta E / dR| = |F / \Delta E|$ , where  $F = d \Delta E / dR$ , corresponds to the critical (crossing) point. Figure 15(c) represents inverse of the gradient  $\beta$ ,  $1/\beta = \Delta E / |F|$ . As shown in the figure, the quantity  $\Delta E / |F|$  has a minimum value at  $R = 0.875$  Å, where  $\Delta E = 5.76$  eV and  $\Delta S = 34.0$  eV/Å. Assuming  $V_{12} = \Delta E / 2 = 2.88$  eV at  $R_c = 0.875$  Å, we could estimate the crossing parameters from the *ab initio* potentials, which are given in Table I as MCSCF2. The crossing parameters  $V(R_c)$  and  $V_{12}^2 / \Delta S$  estimated by assuming empirical relation agree well with the experiments. One has to notice that the scattering angle  $\theta$  is related to the potential height  $V(R_0)$  at closest approach by  $E_{\text{lab}} \theta \approx AV(R_0)$ , which was mentioned above. Then the crossing parameter determined directly from the experimental threshold angle  $\theta_c$  is the potential height  $V(R_c)$  rather than the distance  $R_c$ .

As a concluding remark, the angular and energy dependences of the experimental DCS of the charge-exchange reaction are quite similar to those of the DCS's for the transitions due to the avoided-crossing interactions [3–5]. The critical distance  $R_c$  deduced from the experiments, however, is distinctly larger than the minimum location  $R_{\min}$  in the *ab initio* difference potential  $\Delta E(R)$ , which is different from the well-known relation  $R_c = R_{\min}$  for the avoided-crossing case. The difference  $\Delta R = R_c - R_{\min}$  depends directly on the curvature of the potential  $\Delta E(R)$  around  $R_{\min}$ . The discrepancy in the distance  $R_c$  should be originated from the fact that the reaction in the  $\text{Li}^+$ -Ar collisions takes place through the non-crossing interaction.

As discussed above, the angular dependence of the experimental DCS for the product  $\text{Li}(2p)$  has a broad structure

TABLE IV. Comparison of the crossing parameters for one-electron charge transfers in the collisions of alkali ions with Ar atoms deduced from the experiments.

System	$R_c$ (Å)	$V(R_c)$	$V_{12}^2/\Delta S$ (eV Å)	$r_i+r_j$ (Å)
Li <sup>+</sup> -Ar	0.81	47.0	0.240	0.86
Na <sup>+</sup> -Ar <sup>a</sup>	1.07	46.2	0.361	0.96
K <sup>+</sup> -Ar <sup>b</sup>	1.19	40.5	0.0074	1.30

<sup>a</sup>Kita *et al.*, Ref. [6].

<sup>b</sup>Kita, Izawa, and Inouye, Ref. [5(a)].

which resembles that of reaction (1) for direct excitation of Ar atoms. Therefore, reaction (3b) is considered to proceed through interaction between the potentials for reactions (3b) and (1). In order to discuss this transition mechanism further, one has to evaluate the coupling between the Li( $2p$ ) and Ar( $4p$ ) states.

The experimental crossing parameters for the charge-exchange reaction of one-electron process in the Li<sup>+</sup>-Ar collisions are compared with those for Na<sup>+</sup>-Ar and K<sup>+</sup>-Ar collisions in Table IV. The crossing parameter  $V_{12}^2/\Delta S$  for the asymmetric systems of Li<sup>+</sup>-Ar and Na<sup>+</sup>-Ar has nearly the same value, while that for quasisymmetric K<sup>+</sup>-Ar system has a very small value. For the asymmetric systems the electronic transitions take place through the noncrossing interactions, while the transition for K<sup>+</sup>-Ar is ascribed to the avoided crossing. Thus the excitation mechanisms for the asymmetric and quasisymmetric systems are completely different. Nevertheless, the system dependence of the crossing distance  $R_c$  can be well reproduced by the sum of the ionic and atomic radii  $r_i+r_j$ , as seen in the table. A more impressive feature is that the potential height  $V(R_c)$  at the critical point for the alkali-ions-Ar systems is almost the same, depending only weakly on the system.

### B. Charge-exchange reactions with target excitation

The open circle  $C_3$  (or  $C_4$ ) in Fig. 14 is the experimental adiabatic potential at the crossing point for the charge-exchange reaction with target excitation, and is located between MCSCF curves 4 and 5. Both curves have a minimum around  $R=0.73$  Å, which is nearly equal to the experimental critical distances  $R_{c3}=0.74$  Å (model 1) and  $R_{c4}=0.75$  Å (model 2). As can be seen in Table III, around the distance  $R_{c3}$  (or  $R_{c4}$ ) $\approx 1.4$  a.u., the main configurations for the ground state, and states 2 and 3 are the same as those at the large distance  $R=20$  a.u. On the other hand, characters of the wave functions of the highly excited states 4–7 strongly depend on the distance. At  $R=1.4$  a.u., the wave functions of states 4 and 5 have the main configurations Li<sup>-</sup>( $2s^2$ )+Ar<sup>2+</sup>( $3p^4$ ) and Li( $2s$ )+Ar<sup>+</sup>( $3p^4 4s$ ), respectively. Curve 4 adiabatically leads to the exit channel of Li( $2s$ )+Ar<sup>+</sup>( $3s 3p^6$ ), which was not observed in the TOF measurements. Furthermore, the negative ions Li<sup>-</sup> produced by the reactions could not be detected in the experiments. The potential curve 5 leads adiabatically to the exit channel of Li<sup>+</sup>+Ar( $3s 3p^6 4s$ ), which corresponds to reaction (2a) observed experimentally. Charge transfer with target excitation, therefore, is considered to take place through the tran-

sition onto potential curve 5, followed by the transition from curve 5 to curves 6 and 7. Reaction (2a) was observed only at the lower energies of  $E_{\text{lab}} < 1000$  eV. This suggests that probability of the transition from state 5 to states 6 and 7 is large at higher energies.

### C. Excitations at intermediate and smaller distances

In the Na<sup>+</sup>-Ar collisions studied previously, two different types of electronic transition could be observed [6]. The critical distances for the transitions were close to the distances  $|r_i \pm r_j|$  evaluated from the ionic and atomic radii  $r_i$  and  $r_j$ . As discussed above, the experimental crossing distance  $R_c=0.81$  Å for one-electron charge transfer in Li<sup>+</sup>-Ar is nearly equal to  $r_i+r_j=0.86$  Å. If the transitions in the Li<sup>+</sup>-Ar collisions are similar to those of Na<sup>+</sup>-Ar, another critical distance for Li<sup>+</sup>-Ar is  $R_c=|r_i-r_j|=0.48$  Å, which corresponds to the threshold angle  $(E_{\text{lab}}\theta)_2 \approx 18$  keV deg, evaluating from the deflection function. In the angular dependences of the DCS's for one-electron transitions, we cannot appreciably find the additional structure due to the transitions around the angle  $(E_{\text{lab}}\theta)_2$ . As can be seen in Figs. 7, 8, and 11, the angular dependences of the DCS's for two-electron transitions have single maximum at the lower energies of  $E_{\text{lab}} < 1000$  eV, while they have double maxima for  $E_{\text{lab}} \geq 1500$  eV, which is especially clear in the DCS  $\sigma(\theta)_{B2}$  of the charge transfer with target excitation at  $E_{\text{lab}}=2000$  eV in Fig. 11. If the additional structure observed around  $E_{\text{lab}}\theta \sim 30$  keV deg in Fig. 11 is attributed to the crossing at the intermediate distance, the critical distance is estimated to be  $R_c \approx 0.47$  Å [ $V(R_c) \approx 193$  eV], which is nearly equal to  $|r_i-r_j|=0.48$  Å.

According to the MO correlation diagram for Li<sup>+</sup>-Ar estimated with the *ab initio* computations, the electronic transitions due to  $3d\sigma$  promotion are considered to take place at distances of  $R < 0.5$  a.u. (0.26 Å) [8]. As discussed above, the probabilities of transitions due to interactions at large distances are so high at higher collision energies and large angles that we cannot distinctly determine the crossing point at smaller distance from the experimental results. The energy-transfer spectra of Li<sup>+</sup>-Ar measured at  $E_{\text{lab}}=2000$  eV and  $\theta > 55^\circ$ , however, have a shoulder around  $Q \approx 45$  eV, which was not observed at small angles. Furthermore, the angular dependence of the DCS  $\sigma(\theta)_{2e}$  of two-electron transitions for  $E_{\text{lab}}=2000$  eV in Fig. 9 shows a change in slope around  $60^\circ$ . These features will be ascribed to the avoided crossing at small distance. The turning point for the scattering into  $\theta=60^\circ$  at  $E_{\text{lab}}=2000$  eV is  $R_0 \approx 0.2$  Å, which is close to the crossing distance  $R_c \approx 0.26$  Å estimated theoretically by Barat *et al.* [8].

The MCSCF calculations in this study show that the main configurations of the wave functions of states 1, 2, and 3 at a distance of  $R=0.5$  a.u. are still the same as those at large distances. At  $R=0.4$  a.u., however, the wave functions of states 2 and 3 have the main configurations of Li( $2s$ )+Ar<sup>+</sup>( $3s 3p^6$ ) and Li<sup>+</sup>+Ar( $3s 3p^6 4s$ ), respectively, as shown in Table III. The wave function of state 1 at this short distance still has the same configuration as for large distances, but the contribution of the second configuration of

$\text{Li}^+ + \text{Ar}(3s3p^64s)$  increases steeply at  $R \leq 0.5$  a.u. These results can be interpreted by the MO correlation diagram. The promoted  $3d\sigma$  MO diabatically correlates to the Li  $1s$  AO [see Fig. 7(b) in Ref. [8]]. Excitation of  $\text{Li}^+$  ions could not be observed experimentally at the collision energies of  $E_{\text{lab}} \leq 2000$  eV, but the Ar  $3s$  AO, which correlates to  $3s\sigma$  MO, is promoted around  $R = 0.4$  a.u. ( $\approx 0.2$  Å). This suggests that the crossing of the  $3d\sigma$  and  $3s\sigma$  MO's is strongly avoided, resembling the case of He-Ar [9]. The change in the excitational features observed in the experiments around the distance  $R = 0.2$  Å, which is nearly equal to the radius  $r_i = 0.19$  Å of the  $\text{Li}^+$  ion, will be ascribed to transitions due to the avoided crossing of the  $3d\sigma$  and  $3s\sigma$  MO's.

## VI. SUMMARY

Electronic transitions in the  $\text{Li}^+$ -Ar collisions are observed at energies of  $E_{\text{lab}} \geq 200$  eV. For lower energies of  $200 \leq E_{\text{lab}} \leq 350$  eV, inelastic signals due only to one-electron transitions could be detected, while at  $E_{\text{lab}} \geq 500$  eV two-electron transitions as well as one-electron transitions were observed. In both one- and two-electron transitions, the dominant processes are due to the charge-exchange reactions. According to the analysis of the one-electron charge-transfer DCS by assuming the two-state approximation, the electronic transitions in the  $\text{Li}^+$ -Ar collisions take place at distances of  $R \leq R_c = 0.81$  Å. The potential parameters at the

critical distance for the one-electron charge transfer could be evaluated from the *ab initio* potentials, which reproduce the experimental parameters well. The angular dependence of the DCS's of the two-electron excitations at higher energies of  $E_{\text{lab}} \geq 1500$  eV shows three different types of transitions. The critical distances for the two-electron transitions are  $R_c = 0.75, 0.47,$  and  $0.2$  Å, which are related to the ionic and atomic radii  $r_i$  and  $r_j$ .

The experimental findings in this study are expected to be valid for closed-shell and quasi-one-electron (alkali-atom-closed-shell-atom) systems, but the main part of the findings, i.e., excitation mechanisms, is definitely different from those for symmetric and quasisymmetric closed-shell systems and quasi-one-electron systems.

## ACKNOWLEDGMENTS

We are grateful to Professor M. Izawa (National Laboratory High Energy Physics, Tsukuba, Japan) and Dr. H. Tanuma (Tokyo Metropolitan University, Tokyo, Japan) for their contributions to this work. We also gratefully acknowledge Professor H. Nakamura (Institute for Molecular Science, Okazaki, Japan) for valuable discussions. This work was financially supported in part by the Matsuo Foundation and by Grants-in-Aid for Scientific Research from the Ministry of Education, Science, and Culture of Japan.

- 
- [1] J. C. Mouzon, Phys. Rev. **41**, 605 (1932).  
 [2] V. V. Afrosimov, Yu. S. Gordeev, V. M. Lavrov, and V. K. Nikulin, in *Abstracts of Papers, Proceedings of the Seventh International Conference on the Physics of Electronic and Atomic Collisions, Amsterdam, 1971*, edited by L. M. Branscomb *et al.* (North-Holland, Amsterdam, 1971), p. 143.  
 [3] D. C. Lorents and G. M. Conklin, J. Phys. B **5**, 950 (1972); J. C. Brenot, D. Dhuicq, J. P. Gauyacq, J. Pommier, V. Sidis, M. Barat, and E. Pollack, Phys. Rev. A **11**, 1245 (1975); V. V. Afrosimov, Yu. S. Gordeev, and V. M. Lavrov, Zh. Eksp. Teor. Fiz. **68**, 1715 (1975) [Sov. Phys. JETP **41**, 860 (1976)]; J. Ø. Olsen, T. Andersen, M. Barat, Ch. Courbin-Gaussorgues, V. Sidis, J. Pommier, J. Agusti, N. Andersen, and A. Russek, Phys. Rev. A **19**, 1457 (1979).  
 [4] J. P. Gauyacq, J. Phys. B **9**, 2289 (1976); V. Sidis, N. Stolterfoht, and M. Barat, *ibid.* **10**, 2815 (1977); J. P. Gauyacq, *ibid.* **11**, 85 (1978).  
 [5] (a) S. Kita, M. Izawa, and H. Inouye, J. Phys. B **16**, L499 (1983); (b) S. Kita, H. Tanuma, and M. Izawa, *ibid.* **20**, 3089 (1987).  
 [6] S. Kita, T. Hasegawa, H. Tanuma, and N. Shimakura, Phys. Rev. A **52**, 2070 (1995).  
 [7] N. Andersen, T. Andersen, K. Bahr, C. L. Cocke, E. H. Pedersen, and J. Ø. Olsen, J. Phys. B **12**, 2529 (1979); K. H. Blattmann, M. Dold, W. Schäuble, L. Zehnle, and V. Kempter, *ibid.* **13**, 3389 (1980); R. Düren, H. Hübner, S. Kita and U. Krause, J. Chem. Phys. **85**, 2751 (1986).  
 [8] M. Barat, D. Dhuicq, R. Francois, and V. Sidis, J. Phys. B **6**, 2072 (1973).  
 [9] J. C. Brenot, D. Dhuicq, J. P. Gauyacq, J. Pommier, V. Sidis, M. Barat, and E. Pollack, Phys. Rev. A **11**, 1933 (1975); R. Albat and B. Wirsam, J. Phys. B **10**, 81 (1977).  
 [10] L. D. Landau, Phys. Z. Sowjetunion **2**, 46 (1932); C. Zener, Proc. R. Soc. London, Ser. A **137**, 696 (1932).  
 [11] N. Rosen and C. Zener, Phys. Rev. **40**, 502 (1932); Yu. N. Demkov, Zh. Eksp. Teor. Fiz. **45**, 195 (1963) [Sov. Phys. JETP **18**, 138 (1964)]; T. R. Dinterman and J. B. Delos, Phys. Rev. A **15**, 463 (1977); J. Grosser, Chem. Phys. **30**, 187 (1978); R. Suzuki, H. Nakamura, and E. Ishiguro, Phys. Rev. A **29**, 3060 (1984).  
 [12] H. Inouye, M. Izawa, S. Kita, K. Takahashi, and Y. Yamato, Bull. Res. Inst. Sci. Meas. Tohoku Univ. **32**, 41 (1984).  
 [13] M. Izawa, S. Kita, and H. Inouye, J. Appl. Phys. **53**, 4688 (1982).  
 [14] S. Kita, S. Furusawa, H. Tanuma, I. Kusunoki, and M. Ishigame, Bull. Res. Inst. Sci. Meas. Tohoku Univ. **37**, 33 (1988).  
 [15] S. Kita and H. Inouye, J. Mass Spectrom. Soc. Jpn **41**, 211 (1993).  
 [16] K. Jørgensen, N. Andersen, and J. Ø. Olsen, J. Phys. B **11**, 3951 (1978).  
 [17] H. Inouye and S. Kita, J. Phys. Soc. Jpn. **34**, 1588 (1973).  
 [18] O. B. Firsov, Zh. Eksp. Teor. Fiz. **24**, 279 (1953); G. H. Lane and E. Everhart, Phys. Rev. **120**, 2064 (1960).  
 [19] R. E. Olson and F. T. Smith, Phys. Rev. A **3**, 1607 (1971).  
 [20] C. Zhu and H. Nakamura, J. Chem. Phys. **102**, 7448 (1995).  
 [21] M. W. Schmidt, K. K. Baldrige, J. A. Boatz, J. H. Jensen, S. Koseki, M. S. Gordon, K. A. Nguyen, T. L. Windus, and S. T. Elbert, Quantum Chem. Prog. Exch. Bull. **10**, 52 (1991).

- [22] A. D. McLean and G. S. Chandler, *J. Chem. Phys.* **72**, 5639 (1980).
- [23] Y. S. Kim and R. G. Gordon, *J. Chem. Phys.* **60**, 4323 (1974); V. K. Nikulin and Yu. N. Tsarev, *Chem. Phys.* **10**, 433 (1975).
- [24] S. Kita, K. Noda, and H. Inouye, *J. Chem. Phys.* **64**, 3446 (1976).
- [25] G. Herzberg, *Molecular Spectra and Molecular Structure I. Spectra of Diatomic Molecules* (Van Nostrand Reinhold, New York, 1950), p. 283.